








# Constraining the Systematics of (Acoustic) Wave Heating Estimates in the Solar Chromosphere

Momchil E. Molnar<sup>1,2,3,5</sup> , Kevin P. Reardon<sup>1,2</sup> , Steven R. Cranmer<sup>2,3</sup> , Adam F. Kowalski<sup>1,2,3</sup> , and Ivan Milić<sup>1,4</sup> 

<sup>1</sup>National Solar Observatory, Boulder, CO 80303, USA; [mmolnar@ucar.edu](mailto:mmolnar@ucar.edu)

<sup>2</sup>Department of Astrophysical and Planetary Sciences, University of Colorado, Boulder, CO 80309, USA

<sup>3</sup>Laboratory for Atmospheric and Space Physics, University of Colorado, Boulder, CO 80303, USA

<sup>4</sup>Astronomical Observatory, Belgrade, Serbia

Received 2022 November 8; revised 2023 January 18; accepted 2023 February 6; published 2023 March 16

## Abstract

Acoustic wave heating is believed to contribute significantly to the missing energy input required to maintain the solar chromosphere in its observed state. We studied the propagation of waves above the acoustic cutoff in the upper photosphere into the chromosphere with ultraviolet and optical spectral observations interpreted through comparison with 3D radiative magnetohydrodynamic Bifrost models to constrain the heating contribution from acoustic waves in the solar atmosphere. Sit-and-stare observations taken with the Interface Region Imaging Spectrograph and data from the Interferometric BIdimensional Spectrograph were used to provide the observational basis of this work. We compared the observations with synthetic observables derived from the Bifrost solar atmospheric model. Our analysis of the Bifrost simulations show that internetwork and enhanced-network regions exhibit significantly different wave-propagation properties, which are important for accurate wave flux estimates. The inferred wave energy fluxes based on our observations are not sufficient to maintain the solar chromosphere. We point out that the systematics of the modeling approaches in the literature lead to differences which could determine the conclusions of this type of study, based on the same observations.

*Unified Astronomy Thesaurus concepts:* [Quiet solar chromosphere \(1986\)](#); [Solar chromospheric heating \(1987\)](#); [Radiative transfer \(1335\)](#)

## 1. Introduction

The solar chromosphere has a higher temperature than expected from radiative equilibrium (Withbroe & Noyes 1977; Carlsson et al. 2019). The additional heating required to maintain the chromosphere in its observed thermodynamic state is approximately a few to tens of kilowatts per square meter, depending on the activity of the particular solar feature (Athay 1976; Díaz Baso et al. 2021). Understanding the primary heating sources is important for modeling the solar chromosphere correctly, as these will determine its structure and observed properties. This is an important astrophysical question beyond the Sun, because stellar chromospheres are the source of the ultraviolet (UV) continuum that influences their surrounding environment, for example by dictating the atmospheric chemical composition of their exoplanets (Linsky 2017).

Previous work has suggested that the two most viable mechanisms to provide the missing heating in the solar atmosphere is through stochastic release of stored magnetic energy or dissipation of magnetohydrodynamic (MHD) waves in the solar atmosphere. Release of magnetic energy, either through current-sheet dissipation (Socas-Navarro 2005; Louis et al. 2021) or magnetic reconnection (Innes et al. 1997; Rouppe van der Voort et al. 2017), has been reported throughout the chromosphere with limited global heating implications. Conclusive observational

evidence of this heating process is still lacking, even if models predict it to be pervasive in the active Sun (da Silva Santos et al. 2022).

In this paper we focus on the other possible heating mechanism: acoustic wave energy dissipation. Chromospheric heating by waves was proposed in the late 1940s (Biermann 1946; Schatzman 1949) and has been discussed extensively in the literature (see Aschwanden 2019 for a short review). Recent progress on constraining the wave heating in the solar chromosphere has been enabled by the technological advances of adaptive optics, tunable filtergraphs, and more sensitive UV and near-infrared (near-IR) instruments. There are two differing conclusions about the energetic significance of acoustic waves in the lower solar atmosphere. In general, the body of work based on high-cadence Doppler velocity observations interpreted with a 1D static atmospheric perturbative approach derive wave fluxes sufficient to maintain the quiet chromosphere (e.g., Bello González et al. 2009; Sobotka et al. 2016; Abbasvand et al. 2020b). On the other hand, studies based on Doppler velocities and UV/millimeter continuum observations interpreted with 1D time-dependent radiative hydrodynamic models, well suited for chromospheric studies, come to the opposite conclusion: acoustic waves do not carry sufficient energy flux to maintain the quiet chromosphere (Fossum & Carlsson 2005; Carlsson et al. 2007; Molnar et al. 2021). However, the latter studies have been criticized for systematic biases toward underestimating the acoustic flux (Wedemeyer-Böhm et al. 2007).

For this project, we extended the previous work, of Molnar et al. (2021, henceforth Paper I) on determining the acoustic wave flux in the chromosphere with optical observations, with UV data of the low and high chromosphere from the Interface

<sup>5</sup> Currently at the High Altitude Observatory, NCAR.



Region Imaging Spectrograph (IRIS; De Pontieu et al. 2014). We also used 3D instead of 1D radiative MHD (rMHD) models to interpret the wave observations. This could be considered an extension of similar work by Abbasvand et al. (2021), with the inclusions of multiple spectral lines in the IRIS UV spectral sampling interval instead of relying on the wings of the Mg II h and k lines. We argue that the interpretation of the observed oscillatory signals requires the use of 3D MHD models, contrary to the 1D models used in previous work. Wave modeling that relies on 1D semiempirical models (such as those of Fontenla et al. 2011) calculate the properties of the observed waves as perturbations on a static atmosphere, which may be an inaccurate approximation if the dynamical oscillations are maintaining the atmosphere in a dynamic state far from equilibrium (see Bertschinger & Chevalier 1985 for a treatment of a similar physical setting on Mira-like stars).

This paper describes the observed wave properties in the lower and upper chromosphere observed in the UV with IRIS and tries to infer the energy flux of acoustic waves propagating in these regions through comparison with spectral synthesis from 3D rMHD Bifrost models (Gudiksen et al. 2011). We compared those results with diagnostics from the optical part of the spectrum obtained with the Imaging BIdimensional Spectrograph (IBIS; Cavallini 2006). The paper is organized as follows. Section 2 describes the UV and optical observations used throughout the paper; Section 3 presents the derived properties of the power spectra of different diagnostics; Section 4 presents the wave diagnostics derived from synthetic observables from Bifrost MHD enhanced-network models; Section 5 discusses the systematics between different modeling approaches. We conclude with the wave energy flux estimates in Section 6, and discuss the implications of our results in Section 7.

## 2. Observations

To extend the previous work in Paper I, we use UV spectral diagnostics observed with the IRIS spacecraft to sample the upper chromospheric velocity and intensity diagnostics. For this paper, we concentrate on the Mn I 280.108 nm line (lower chromosphere; Pereira et al. 2013), the Mg II h<sub>2</sub> & k<sub>2</sub> features (middle chromosphere), and the Mg II h<sub>3</sub> & k<sub>3</sub> features (upper chromosphere; Leenaarts et al. 2013). The IRIS data archive offers a vast collection of observations containing this spectral line set. We compare the properties of the UV data with the results from Paper I to obtain a new and more complete estimate for the energy fluxes that acoustic waves are carrying and the possible implications for chromospheric heating.

Throughout the paper we will discuss two different types of solar features: internetwork and plage. These regions harbor weak magnetic fields in the case of internetwork and stronger magnetic fields in the case of the plage. The choice of these two types of solar surface is based on their relatively simple discrimination from the rest of the solar structures. Furthermore, in the internetwork features we did not expect the weak magnetic field to be significant for the wave propagation. In the case of the plage, previous work has showed the ubiquity of fluctuation signatures and a mostly vertical magnetic field (Pietrow et al. 2020; Anan et al. 2021), which could harbor MHD wave modes.

**Table 1**  
IRIS Observations Used in This Work

Date	Start (UT)	End (UT)	Cadence (s)	Solar Feature
20131116	07:33	08:08	17.0	Internetwork
20140918	10:19	12:16	9.4	Plage

### 2.1. Processing of the Interface Region Imaging Spectrograph Data

We use the *levl\_2* spectral rasters from the IRIS online data archive<sup>6</sup> for this analysis. The particular data sets used in this study are described in Table 1. We chose two sets of observations from the earlier stages of the IRIS mission to ensure higher sensitivity and lower noise levels. The data sets used in this work are in sit-and-stare mode, which increases the signal-to-noise ratio of the observations and provides higher Nyquist sampling frequency.

The two UV spectral lines of interest have different shapes: the Mn I 280.1 nm line has a simple absorption profile, whereas the Mg II h & k lines have a complicated, typically double-peaked shape due to the high-opacity nonequilibrium effects at chromospheric heights (Tousey 1967). We adopted different fitting approaches to extract the physical parameters from the two spectral lines. The Mg II h & k lines are fitted with the IDL routine *iris\_get\_mg\_features\_lev2.pro*, part of the SSW IRIS reduction routine suite. This procedure relies on derivative estimates and subpixel interpolation to calculate the locations and amplitudes of the features of the Mg II h & k lines (described in detail in Pereira et al. 2013). In this work we concentrate our analysis on the properties of the k<sub>3</sub> and h<sub>3</sub> features, which are the central extrema (global maxima or a local minimum) of the line profile, that is, always present, even in the plage region (Tousey 1967). The Mn I 280.1 nm line is situated between the Mg II k and h lines that produce a sloped background continuum. We used the IDL routine *Gaussian\_fit* to fit a combination of a Gaussian plus an inclined line on the wavelength range of  $\pm 0.03$  nm around the line center because the Mn I line has a regular absorption line shape. We derived the line properties from the parameters of the fitted Gaussian profile. Analysis of the Mn I 280.1 nm line and Mg II k feature formed the basis for the study by Kayshap et al. (2018), where the authors found clear signatures of wave propagation throughout the quiet solar atmosphere. The IRIS spacecraft pointing jitter during the sequences is negligible, verified by the cross-correlation of individual slit-jaw frames.

After deriving the fits of the spectral lines and calculating the resulting Doppler velocities and line-core intensities, we cleaned the data from nonconverged line fits, which amounted to a few percent of the total fits. We first removed any nonconverged fit values by replacing them with a  $3 \times 3$  pixel median filter that excludes nearby nonconverged fits pixels. We further smoothed out any discontinuities in the temporal domain in the velocity signal that are above the local sound speed ( $7 \text{ km s}^{-1}$ ) with a  $3 \times 3$  pixel median filter, which corresponds to a  $0''.5 \times 27 \text{ s}$  kernel for the plage and to a  $0''.5 \times 51 \text{ s}$  kernel for the internetwork. The Nyquist frequency of our data is 29 mHz for the internetwork and 51 mHz for the plage data set. In the analysis in Section 3 we show that the frequencies containing valuable information are between 5 and

<sup>6</sup> <https://iris.lmsal.com/data.html>

20 mHz, well below the Nyquist frequency. The spatial smoothing over  $0''.5$  does not affect the estimated wave properties, as previous work utilizing high-resolution data (e.g., Vecchio et al. 2007) has shown that the coherence scale of the velocity signals in the chromosphere is of similar spatial scale (see the bottom two rows of Figure 1). The resulting data products from the aforementioned reduction procedures are presented in Figure 1. The left column shows an internetwork region and the right one presents a plage region, both observed near to the disk center. Because the lower part of the plage field of data set field of view (FOV) is occupied by an internetwork, we exclude this part from the plage analysis. In particular, we use the slit locations between pixels 400 and 705, which are marked in the right column of Figure 1 as the green (red) lines. For the internetwork, we use the full extent of the slit.

## 2.2. Processing of the Imaging Bidimensional Spectrograph Data

This study uses data from the IBIS (Cavallini 2006) instrument, acquired during an Atacama Large Millimeter/submillimeter Array (ALMA) coordinated observing campaign on 2017 April 23. The observed region was centered on the leading edge of AR 12653. The FOV was  $96''$  and included regions of plage, internetwork, network, and penumbra. These observations were taken between 17:25 and 18:12 UT and include scans of the Na I  $D_1$  589.6 nm and the Ca II 854.2 nm line, consisting of 24 and 27 points in each line, respectively, which were described in detail in Hofmann et al. (2022). This data series has a temporal cadence of 16 s and spectral resolution of at least  $R \gtrsim 200,000$  (Reardon & Cavallini 2008). The line cores were more densely sampled than the wings of the spectral lines because the core region is used for deriving the quantities used in this study (Doppler velocities and line-core intensities). The IBIS data processing is described in detail in Molnar et al. (2019), where we have applied the standard reduction techniques of removing instrumental and atmospheric image aberrations and destretching the resulting data to the Helioseismic and Magnetic Imager (HMI) white-light (atmospheric seeing-free) reference (Scherrer et al. 2012). In this work we use the data sets starting at 15:54 UT and 16:37 UT, which were taken under conditions of good seeing.

## 3. Properties of the Observed Power Spectra

We studied the wave dynamics in the observed chromospheric diagnostics by analyzing their power spectra. The power spectra are derived for each pixel in a selected interval along the slit from the squared absolute value of a Fourier transform of the time series, giving us the power spectral density (PSD) of the data. The power spectra of the IRIS data exhibit ubiquitous power-law shapes at frequencies above the acoustic cutoff present in all chromospheric and photospheric observables. These power laws exhibit similar behavior to those previously observed in the chromosphere, for example in Reardon et al. (2008), and will be discussed further below. The average shapes, slopes, and other properties of the power laws are presented in this section.

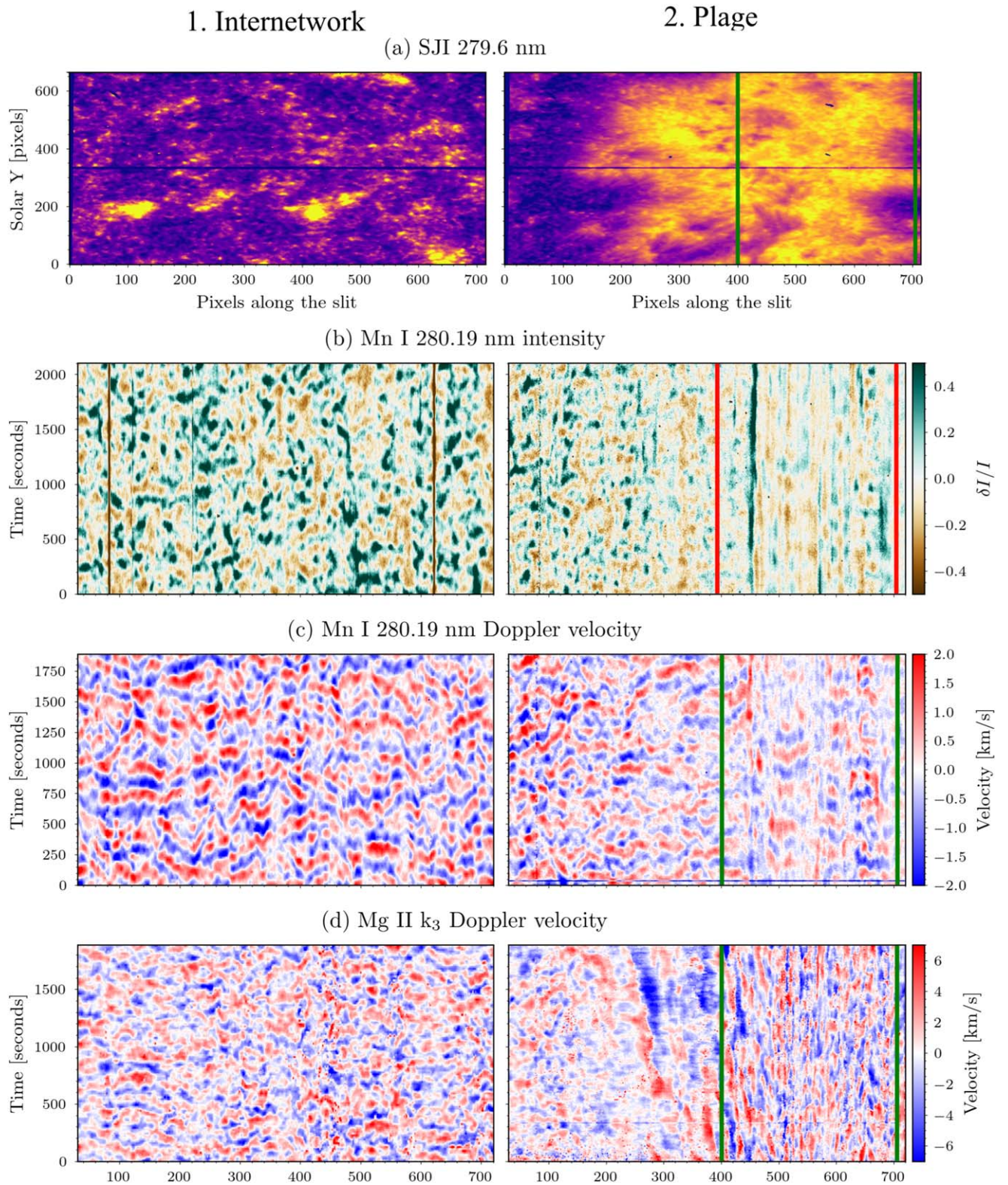
Figure 2 presents the average PSDs and their derived properties for the different solar regions and spectral diagnostics. The average power spectra for the different solar regions are shown in the top panel. The internetwork data exhibits the typical 3 minute (5 mHz) peak in both the Mn I line

(lower chromosphere) and the Mg II k line (upper chromosphere). This can be seen clearly from the last two rows of Figure 1, where the velocity diagnostics of the quiet Sun exhibit a regular pattern with a timescale of about 3 minutes. The plage data exhibit a peak at lower frequencies, around the 3 mHz (5 minute) oscillations (as previously shown by de Pontieu 2004, Morosin et al. 2022, and Sadeghi & Tavabi 2022), which is more pronounced for the lower chromospheric diagnostics. Furthermore, the Doppler velocity observations in the plage (last two rows of Figure 1) do not seem to exhibit the clear oscillatory pattern seen in the internetwork data, which results in a less well-defined peak in their Doppler velocity power spectra.

Zaqarashvili & Skhirtladze (2008) have suggested that the lower-frequency peak in the velocity PSD in the plage regions might be a signature of the kink-wave frequency in the chromosphere. However, we did not find a clear correlation between the cotemporal magnetic field strength in the photosphere measured by the Solar Dynamics Observatory/HMI (Schou et al. 2012) and the peak of the plage velocity PSD, as suggested from the behavior of the kink-wave cutoff. We intend to extend this study to look for the signatures of the kink-wave cutoff frequency complemented with chromospheric magnetic field measurements from DKIST (Rimmele et al. 2020) combined with IRIS observations in a following publication.

To quantify the usable range of frequencies for our analysis, we calculated the white-noise floor, which is clearly seen in Figure 2(a) as the flat, frequency-independent signal at high frequencies. We compute the white-noise floor as the median power above the 25 mHz frequency. This noise-frequency cutoff is outside of the frequency range used for the wave-power analysis. The white-noise floor distributions of the different solar regions are shown in Figure 2(c). Similar to the results in Paper I, we observe that the white-noise floor is slightly higher for the plage when compared with the internetwork regions. We also find that the Mg II-derived diagnostics have a higher white-noise floor compared with the Mn I ones. This trend might be due to the measurement technique and/or the nature of the chromospheric lines in question, as the Mg II lines have a complex shape that requires an elaborate fitting routine (Pereira et al. 2013). By examining the mean frequency when the power rises above the white-noise level, we define the meaningful frequency region of the PSDs, to be used for further analysis, as 20 mHz for internetwork regions and 12 mHz for the plage regions, because white noise dominates above those frequencies, as clearly seen in Figure 2(a).

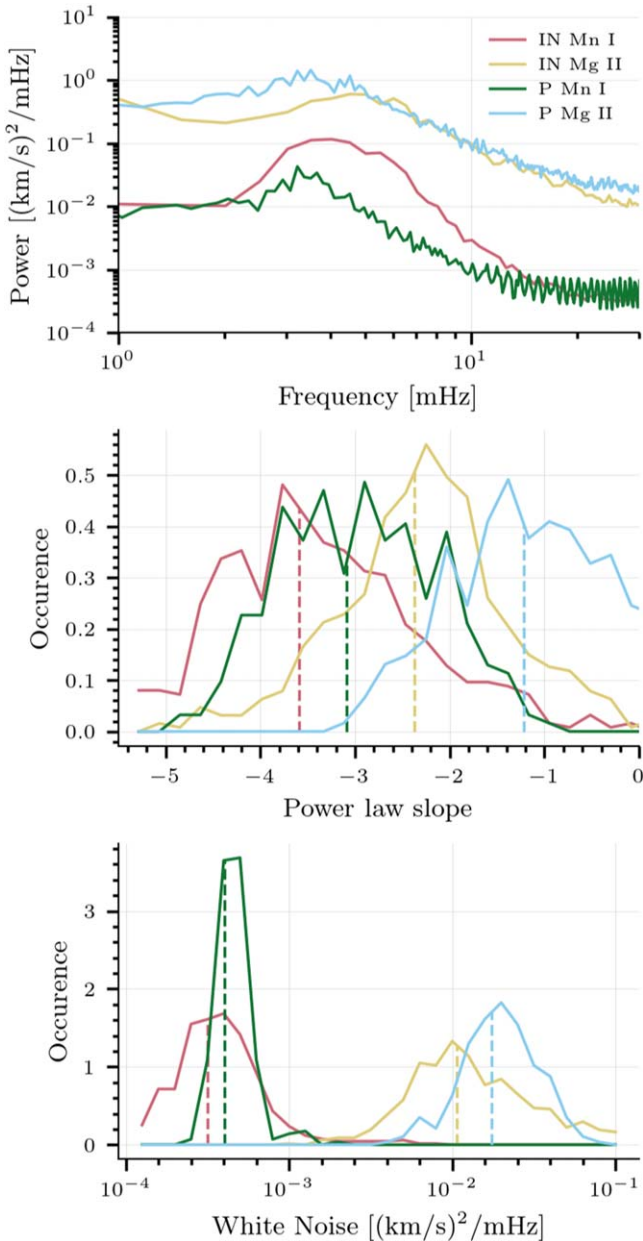
We perform a linear fit on the log-log representation of the velocity PSDs to estimate the power-law slopes. The middle panel of Figure 2 presents the power-law slopes of the observed PSDs for the different regions of interest. For the plage regions we fit the data between 3 and 12 mHz, and for the quiet Sun we fit the interval between 5 and 20 mHz, due to the different levels of white noise discussed in the previous paragraph. The dotted lines show the median of the power-law slope distributions. The power laws of the diagnostics formed in the lower chromosphere exhibit steeper slopes compared to the ones formed in the upper chromosphere. Interestingly, for both IRIS lines the plage exhibits steeper power-law slopes than the internetwork regions, similar to the behavior of the Ca II IR line in Paper I. The slopes of the vertical velocity PSDs are



**Figure 1.** The data used in this study come from two different regions, the internetwork (left column) and plage (right column), where the dark line across the center of the image is the actual slit. The left column shows observations of an internetwork region from 2013 November 16; the right column plage region observations from 2014 September 18 (see Table 1). The top row (a) are slit-jaw images in the 279.6 nm spectral window for the internetwork (left) and plage (right). Row (b) show the relative intensity variations (to the mean intensity at the particular slit position) at the core of the Mn I 280.19 nm line. Rows (c) and (d) show the Doppler velocities derived from the Mn I 280.19 nm line and the Mg II  $k_3$  feature, respectively. All panels present along their  $x$ -axis the slit dimension.

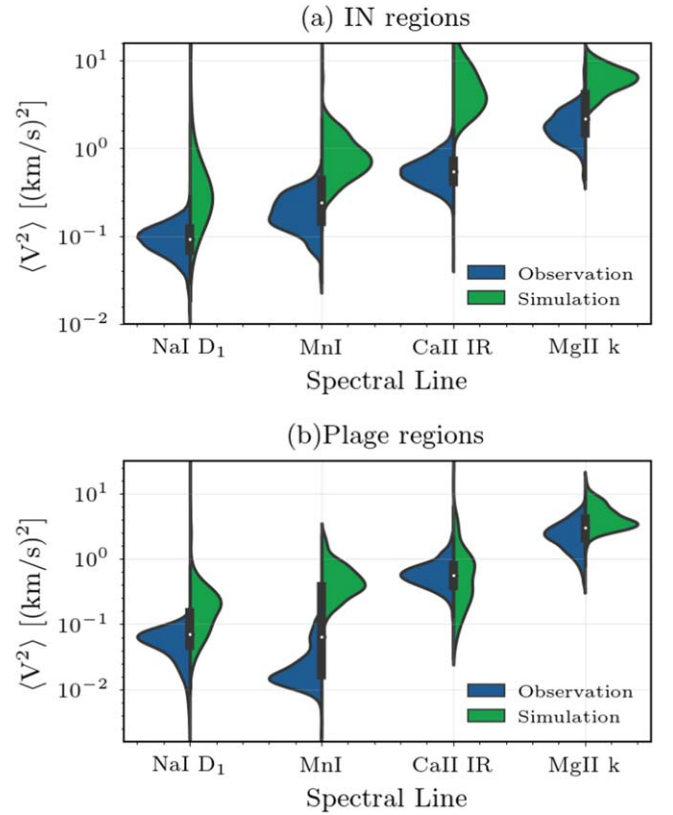
signatures of the wave environment in the chromosphere and they are a crucial dynamic constraint for realistic rMHD models of the solar chromosphere.

Figure 3 shows the integrated Doppler velocity oscillatory power between 5 and 20 mHz in the Mn I and the Mg II  $k_3$  features as the blue distributions. We analyzed only these



**Figure 2.** Observed power spectra and their power-law properties for the different solar regions and spectral diagnostic. Top: average power spectra. Middle: histograms of the slopes of the fitted power laws. Bottom: histograms of the white-noise floors for the different diagnostics. The color-coding is consistent throughout the paper. The analyses of the data presented in this figure are described in detail in Section 3.

frequencies because waves with these periodicities, above the acoustic cutoff frequency (about 5 mHz in the solar photosphere), will be able to propagate upward. The acoustic cutoff frequency varies across the solar atmosphere (Felipe et al. 2018; Jefferies et al. 2019), being lowered at locations with strong magnetic field concentrations (Heggland et al. 2011), but our choice to exclude the power between 3 and 5 mHz is a conservative estimate of the wave flux, which will not change the end result by more than a factor of about 2, which is not enough to change the conclusions of this work, as shown in Section 6. We also degraded the resolution of the synthetic data down to the resolution of the IRIS and IBIS instruments to take into account their diffraction limits.



**Figure 3.** Integrated Doppler velocity oscillation power between 5 and 20 mHz in the IRIS and IBIS diagnostics in the two different solar features (see Section 3), after subtraction of the white-noise floor. The ordering of the spectral lines reflects their relative average height of formation in the solar atmosphere. The blue distributions are real observations, whereas the green distributions are Bifrost-derived synthetic observables.

We also included the amount of oscillatory power from the optical lines of Na I  $D_1$  and Ca II 854.2 nm observed with IBIS. In all cases, for both IRIS and IBIS diagnostics, we have subtracted a local estimate of the high-frequency white-noise component for each pixel, following the noise-estimation procedure described in the previous paragraph. Those IBIS observations were obtained on a different day and region than the IRIS data analyzed here, but we applied feature-selection criteria, described in Paper 1, making for a suitable statistical comparison between these diagnostics. In Figure 3 the blue distributions are derived from observations and the green ones from simulations, which will be described in Section 4.2. The average values of the IRIS velocity fluctuation power are summarized in Table 2.

An increase in the amount of velocity oscillatory power is observed with increasing height in the observations in Figure 3, where the spectral diagnostics are arranged in order of increasing height of formation. This is presumably due to the steeply decreasing density with height in the solar atmosphere, leading to increasing wave amplitudes, even though the actual wave flux may be decreasing with height. We also note that the absolute amount of observed line-of-sight velocity oscillations is higher in the internetwork in the lower chromosphere compared with the plage regions. However, in the middle and upper chromosphere the difference in the amount of velocity oscillation between the internetwork and the plage is diminished.

**Table 2**Average PSD Properties of the Observed Solar Regions in the Two IRIS Lines (Mn I 280.1 nm and Mg II  $k_3$ ) with the 10th/90th Percentile Quoted

Solar Feature Spectral Line	Slope	Noise Floor ((km/s) <sup>2</sup> /mHz)	$\langle v^2 \rangle$ ((km/s) <sup>2</sup> )
IN Mn I	$-3.56^{+1.02}_{-0.89}$	$3.2^{+2.1}_{-1.3} 10^{-4}$	$0.18^{+0.12}_{-0.065}$
IN Mg II $k_3$	$-2.33^{+0.85}_{-0.91}$	$1.1^{+1.7}_{-0.5} 10^{-2}$	$1.76^{+0.97}_{-0.55}$
Plage Mn I	$-3.09^{+0.88}_{-0.81}$	$4.0^{+0.9}_{-0.6} 10^{-4}$	$0.02^{+0.03}_{-0.005}$
Plage Mg II $k_3$	$-1.22^{+0.90}_{-0.86}$	$1.7^{+0.9}_{-0.6} 10^{-2}$	$2.31^{+1.18}_{-0.98}$

**Note.** The amount of oscillatory velocity power is calculated between 5 and 20 mHz with the white noise subtracted. The calculation of the properties is described in detail in Section 3.

The Na I  $D_1$  line velocity data agree well with the velocity data from the Mn I 280.1 nm line, which is unsurprising given that both lines are formed at similar heights on average (Leenaarts et al. 2010; Pereira et al. 2013). The Ca II 854.2 nm line shows velocity fluctuation amplitudes between the Mn I line and Mg II  $k_3$  feature. This confirms that the resulting wave amplitudes, coming from different spectral lines, is self-consistent and presents a uniform physical picture of the amount of wave amplitude in the solar atmosphere.

#### 4. Acoustic Wave Propagation in Solar Simulations: 1D versus 3D Models

The energy flux,  $F_{ac}$ , of propagating acoustic waves with frequencies between  $\nu_{ac}$  (the acoustic cutoff frequency) and an upper-limit frequency  $\nu_1$  can be derived from observations with the following expression (following the derivation in Bray & Loughhead 1974 and Bello González et al. 2009):

$$F_{ac} = \rho \sum_{\nu'=\nu_{ac}}^{\nu_1} \frac{\langle v_{obs}^2(\nu') \rangle}{\mathcal{T}^2(\nu')} v_{gr}(\nu'), \quad (1)$$

where  $\rho$  is the plasma density at the formation height of the observed diagnostic,  $\langle v_{obs}^2(\nu') \rangle$  is the observed velocity variance at frequency bin  $\nu'$ ,  $\mathcal{T}(\nu')$  is the attenuation coefficient due to the finite thickness of the formation region of the spectral line (Mein & Mein 1976), and  $v_{gr}(\nu')$  is the group velocity of the wave mode at frequency  $\nu'$ . To estimate the wave energy flux, we have to evaluate the terms on the right-hand side of Equation (1) from models or observations. The quantity  $\langle v_{obs}^2(\nu') \rangle$  can be obtained from the observations as described in Section 2. The other three quantities, however, need to be estimated from numerical models, as we describe in this section.

We extend previous analyses (Wunnenberg et al. 2002; Fossum & Carlsson 2005; Sobotka et al. 2016) to compare the differences between 1D models (FAL, RADYN) and 3D models (Bifrost). In comparison with 1D models, the Bifrost model includes additional physical processes (dynamical evolution, shock formation, detailed radiative transfer and nonequilibrium ionization of hydrogen) that produce a wealth of small-scale phenomena. This approach allows for a self-consistent description of wave propagation in the chromosphere, avoiding some of the problems with 1D modeling described in Ulmschneider et al. (2005). Previous work by Fleck et al. (2021) compared the general wave-propagation

properties in 3D MHD simulations, including Bifrost, and found a lack of general agreement among the different models. We note that those authors did not explore the observational signatures of high-frequency wave propagation in the chromosphere, which is the central topic of this paper.

#### 4.1. RADYN Models

We use the same RADYN (Carlsson & Stein 1992; Allred et al. 2005, 2015) runs presented in Paper I to interpret the IRIS observations. The initial RADYN atmospheric model used was an internetwork atmosphere model with 191 grid points. The model has a piston-like lower boundary condition that acts as a subphotospheric wave driver and an open upper boundary with constant temperature of 1 MK. RADYN self-consistently solves the equations of radiative transfer, statistical equilibrium, and the hydrodynamic equations, where the code can take into account the time-dependent ionization. Furthermore, the RADYN code treats in non-local thermodynamic equilibrium (non-LTE) the transitions of hydrogen, calcium, and helium with six-, six-, and nine-level atom models, respectively.

We synthesized time series of spectral line profiles from these models. Based on these synthetic observables, we estimated the line displacements and intensities, to be described in the further analysis. To synthesize the Mn I and the Mg II spectral diagnostics studied throughout this work, we used the RH 1.5D code (Uitenbroek 2001; Pereira & Uitenbroek 2015). For the synthesis of the Mn I 280.1 nm line, we used the Kurucz line list database<sup>7</sup> (Kurucz 2018) and we synthesized it in local thermodynamic equilibrium (LTE). We note that the lines of Mn I exhibit non-LTE effects (Bergemann et al. 2019), but we leave the assessment of the importance of these effects for a future work. To synthesize the Mg II h & k lines we used the RH code in non-LTE mode with 10-plus-one Mg III ground levels and partial frequency redistribution taken into account (the same setup used in Leenaarts et al. 2012).

#### 4.2. Bifrost Models

Modern 3D rMHD codes appear to result in increasing levels of realism of the simulated solar atmosphere (Björge et al. 2019). To leverage the advantages of multidimensional rMHD simulations, we used publicly available Bifrost data cubes<sup>8</sup> - from the enhanced network *en024048\_hion* (Gudiksen et al. 2011; Carlsson et al. 2016). In this simulation we utilize the quiet regions as realizations of quiet Sun internetwork and the more active network as representative of plage regions. We further employed publicly available radiative transfer products for the Mg II h & k and the Mn I 280.9 nm lines, which are synthesized with the RH 1.5D code and publicly available for the *en024048\_hion* enhanced network (Pereira et al. 2013). We also synthesized the Ca II 854.2 nm and Na I  $D_1$  lines with RH 1.5D in non-LTE. We used a six-level model atom for the Ca II 854.2 nm line, including a Ca III ground state; for the Na I  $D_1$  line, we used a model atom with four levels that includes a Na II ground state.

Before proceeding with the analysis of the spectral synthesis products, we note a few deficiencies of the Bifrost models which should be kept in mind when interpreting the following

<sup>7</sup> <http://kurucz.harvard.edu/linelists.html>

<sup>8</sup> Available at <http://sdc.uio.no/search/simulations>.

results. First, the UV solar spectrum is not well reproduced, with spectral features lacking in intensity and width (Pereira et al. 2013). As discussed previously in Carlsson et al. (2016), this might be due to a combination of factors, such as insufficient heating in the chromosphere and corona and the lack of small-scale motions in the simulated atmospheres. The other major drawback of these models is the presence of global oscillations over the whole simulation domain with velocity perturbations on the order of a few kilometers per second in the lower chromosphere, accompanied by density fluctuations on the order of 20% (described previously in Carlsson et al. 2016 and Fleck et al. 2021). We have attempted to remove the signature of these wave modes in our analysis by filtering them in temporal Fourier space, given their periods are lower (about 10 minutes) compared with the periods of interest in this paper and are coherent over the whole domain.

### 4.3. Properties of the Synthetic Observables from Bifrost

Figure 4 shows the formation properties of the Mn I 280.1 nm line (top panel) and Mg II  $k_3$  (middle panel) in the enhanced-network Bifrost simulation. Figures 4(a) and (e) show the height of optical depth unity, referred to as the height of formation of the spectral line. These panels indicate that the two spectral lines are formed at significantly varying heights in the atmosphere at different locations in the FOV, as previously shown in Pereira et al. (2013). This spread of the height of formation is a significant contribution to the broad distribution of densities at the  $\tau = 1$  heights, which are shown in Figures 4(b) and (f). This raises the question of the applicability of the approach based on inferring the acoustic flux using a singular density value for a given spectral line. Additionally, the effective height of formation of a spectral line may change as the atmospheric properties evolve in time. The amplitude of this effect is illustrated in Figures 4(c) and (g), which show for each line the ratio of the difference between the 10th and 90th percentile of the temporal density variation to the time-averaged plasma density at the height of formation for each pixel. We note a strong temporal variation of the density at the height of formation with time on the order of a factor of a few for the same temporal location, similarly to Felipe & Socas-Navarro (2023). This change is due to the passing wave fronts and the different amplitudes are due to the significantly different properties of formation of the diagnostics in the two regions. For the Mn I line, the density of formation changes by an order of magnitude in internetwork regions over time, but relatively less in the enhanced-network regions. For the Mg II  $k$  line, we see that the density changes most significantly along the fibrillar structures, connecting the two magnetic regions in the simulation domain.

Based on the spectral synthesis of the two UV and the two optical lines, we computed  $\tau = 1$  plasma density histograms for each spectral line from the first snapshot of the simulation. Panel (i) shows that the densities at the  $\tau = 1$  heights exhibit wide distributions that present a challenge for the computation of the wave fluxes. If we examine indicative enhanced-network (magenta squares in panels (a) and (e)) and internetwork (green squares in panels (a) and (e)) structures we find that those regions exhibit almost constant density inside the small boxes. The average of the density from those regions could be used as the representative of the values to be used in Equation (1) when estimating the acoustic fluxes. This strong dependency of the density on the particular solar region, further described in

Section 5, makes providing an accurate model for every solar feature crucial for the accurate estimation of the wave flux.

The acoustic wave flux present in the simulation cube can be computed at different heights as the plasma conditions are known. Due to the varying formation conditions of the diagnostics, described in the previous paragraph, we estimated the average height of formation for each spectral line separately for each column of the simulation. Based on the average height of the column, we extracted the average plasma density and the amount of vertical velocity oscillatory power between 5 and 20 mHz at that height in the simulation. Based on these estimates, we computed the average wave flux at the local formation height of the spectral lines. The resulting acoustic wave flux distributions for all spectral lines are presented in panel (j) of Figure 4. The amount of acoustic flux with height decreases significantly, in contrast to the almost constant amount of wave flux in the 1D RADYN chromosphere (Fossum & Carlsson 2006). This is the typically observed behavior of the wave flux with height, as hinted by previous observations (e.g., Abbasvand et al. 2020b). The amount of acoustic wave flux in the Bifrost simulation chromosphere resembles the results based on the RADYN models in Paper I, but exhibit a more realistic decrease of the wave flux with height (Ulmschneider et al. 2005). This is further described in detail in Section 4.3.

Based on the spectral profiles computed from the Bifrost simulation, we measured the Doppler velocities using the same procedure as for the real observations, described in Section 2.1. We have also subtracted a white-noise estimate, derived as frequency independent at high frequencies of the power spectrum. We compare the amounts of Doppler velocity fluctuations in the real data (blue distributions) and the simulations (green distributions) in Figure 3. The data for the simulation results are based on the aforementioned green and pink regions in Figure 4. The simulations seem to exhibit significantly higher-velocity oscillation power than the actual Sun, often up to a magnitude more.

The acoustic wave energy propagating through the chromosphere appears to be mostly dissipated by the time it reaches the height of formation of the Mg II  $k_3$  feature (see Figure 4(h)) in the simulations. This is further illustrated in Figure 5, where the height dependence of the acoustic flux in the internetwork and magnetic concentration regions are shown. The amount of velocity variance is also shown in Figure 5 as the dashed lines. We can see that the amounts of vertical velocity oscillatory power in the internetwork and the plage are similar in the photosphere, but in the chromosphere the internetwork has higher-velocity oscillation power by a factor of 2. However, when taking into account the slightly lower density at chromospheric heights for the internetwork, compared with the enhanced network, we found that the velocity amplitudes are almost the same over a large range of heights.

This analysis shows the drawbacks of using 1D atmospheric models to infer the wave fluxes. First and foremost, perturbative approaches (such as in Bello González et al. 2009 and Abbasvand et al. 2020b) cannot account for the atmospheric properties changing significantly between different solar features. Previous work by Fossum & Carlsson (2005, 2006) used time-dependent 1D HD RADYN models to infer wave fluxes from TRACE observations, but these authors did not use differing starting atmospheric models to study the behavior of different solar features, or have used

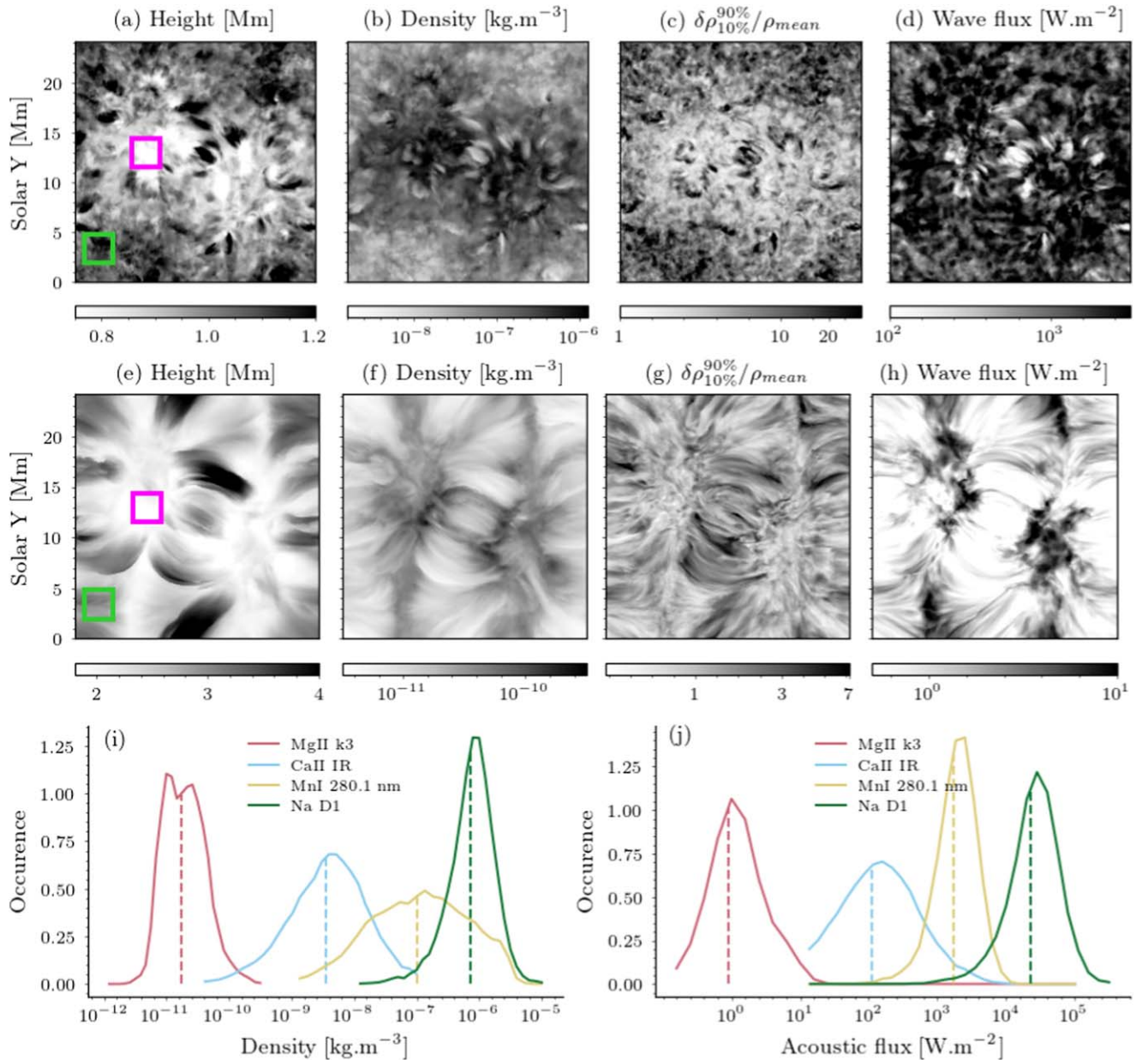


**Figure 4.** Results from the Bifrost spectral synthesis. The top row shows diagnostics derived from the Mn I 280.1 nm line and the middle row shows those for the Mg II  $k_3$  feature. Panels (a) and (e) show the time-averaged height of optical depth unity of the line core, panels (b) and (f) the time-averaged density at optical depth unity for the line core, panels (c) and (g) show the ratio of the plasma density change over time to the mean plasma density at the formation height of the spectral lines, and panels (d) and (h) the acoustic flux at the formation height of the spectral line. The green and magenta squares in panels (a) and (e) are the representative regions that we equate to internetwork and plage regions in our observables in the following analysis. The bottom-left panel (i) shows the distributions of the density at the height of formation in the simulation for the different diagnostics; the bottom-right panel (j) shows the distributions of the acoustic flux at the height of formation of the diagnostics.

multiple 1D semiempirical static models (Sobotka et al. 2016). Furthermore, analysis of the 3D models shows that the high-frequency waves do not oversaturate the chromosphere with acoustic power as in the 1D case (Ulmschneider et al. 2005).

A key property that affects the estimation of the acoustic flux is the plasma density. We do not argue about the veracity of the conclusions in either approach, as the reliability of 3D models to represent the wave dynamics of the solar atmosphere is still under debate (Fleck et al. 2021). Furthermore, the too-weak spectral lines in the synthetic spectra are most probably due to low densities in the Bifrost simulations (Carlsson et al. 2016). In the next section, we compare the different modeling approaches, quantifying their systematic differences, which

might explain some of the discrepancies among the previous results for acoustic flux estimates.

## 5. Systematics of Acoustic Wave-flux Estimation from 3D versus 1D Models

The spectral synthesis of observables from numerical solar models provides us with a direct way to examine how the variations in measured diagnostics relate to the actual changes in atmospheric plasma properties. In this section we examine the behavior of the following components of Equation (1) in different modeling approaches: (i) atmospheric velocity at height corresponding to the observed Doppler velocity



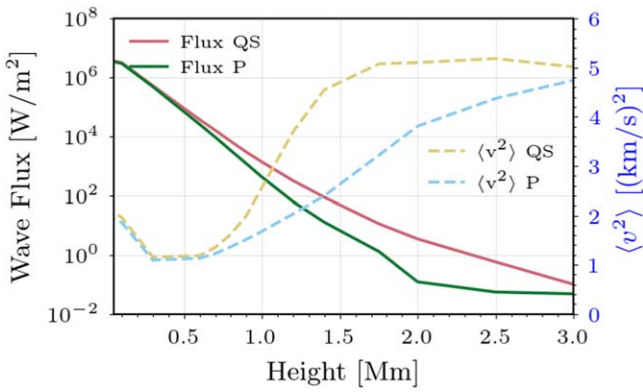


**Figure 5.** Height variation of the acoustic flux and vertical velocity fluctuation amplitude between 5 and 20 mHz in the Bifrost model for internetwork (green) and plage regions (red). The solid (dotted) lines show the wave flux (velocity fluctuation). The regions of the simulation used are shown in panels (a) and (e) of Figure 4 as the colored squares.

measurement and ascertaining the source of the observed velocity fluctuations, whether true plasma motions or rather changes in the  $\tau = 1$  surface; (ii) the density at the height of formation associated with the oscillatory signal; and (iii) the transmission coefficient in different regions of the solar atmosphere. We compare the results from the 3D Bifrost simulations with previous results from RADYN and FAL atmosphere-based modeling (Fontenla et al. 2011). Such comparison allows for estimating the systematic errors that are introduced by using a particular modeling approach. This is an important aspect of these studies that has not been well constrained previously. We demonstrate that the specific choices made for the height of formation, density, and transmission coefficient can drastically change the conclusions of these studies.

### 5.1. Measuring Velocity Fluctuations, but Where?

The analysis in Section 4.3 shows that the Doppler velocity signals derived from synthetic spectral lines originate from a height that can change with time and depending on the underlying solar feature. Hence, we need to determine at which height the Doppler velocity samples the true vertical velocity field most closely.

To constrain to which height the observed Doppler velocity relates to, we calculated the Pearson correlation coefficient between the observed Doppler velocity and the plasma vertical velocity. The highest correlation coefficient values were found at the heights of the time-averaged optical depth unity, which confirmed our previous calculations.

We compared the Doppler velocities in the synthetic spectral observations with the acoustic flux at the  $\tau = 1$  height of formation of the spectral line. The results are shown in Figure 6, where the first row is for the Mn I line and the second row is the Mg II  $k_3$  feature. Optimally, there would be a direct mapping between  $v_{\text{obs}}^2$  and the wave energy flux, which would imply that the estimation of the density and the attenuation coefficient should be straightforward.

For both spectral lines there is a good agreement between the distribution of the observed synthetic velocity oscillations and the true vertical velocity oscillations at the line height of formation in the solar atmosphere. Panels (a) and (b) of Figure 6 show the observed Doppler velocity and the velocity at the time-averaged  $\tau = 1$  height for the Mn I 280.1 nm line.

Panels (e) and (f) show the same for the Mg II  $k_3$  feature. On average, the observed Doppler velocity fluctuations are lower than the true vertical plasma velocities in the solar atmosphere. This is due to a Doppler velocity attenuation effect that smears out the vertical velocity signal in the solar atmosphere. It is caused by a combination of multiple phases of the acoustic waves that might be present in the width of the formation region as well as the changing line height of formation (Mein & Mein 1976). This observed decrease of the wave amplitudes is described by the  $\mathcal{T}$  coefficient, discussed further in Section 5.3. The total amplitudes of the velocities derived from the synthetic observables are on average lower by a factor of 2 to 4, due to the attenuation of the signal.

However, when we compute the acoustic fluxes at the time-averaged  $\tau = 1$  surfaces of the simulations, we see that the correspondence with the velocity amplitudes is mostly nonexistent (panels (c) and (g)). This is due to the fact that the other major component of the acoustic flux calculation is the density. The density at the height of line formation varies significantly in the different regions of the chromosphere, as shown in panels (b) and (f) in Figure 4. In particular, these subfigures show us that the local density changes by more than an order of magnitude between the quiet and enhanced-network regions. This can be understood as in the hotter (network) regions the diagnostics are formed at a lower height and, on average, at higher column mass (Fontenla et al. 2011). The density variation is significantly higher than the variation of the amplitudes of the observed velocity fluctuations in the simulations.

This strong spatial variation of plasma properties results in the poor correlation between the observed synthetic velocity oscillation power and the acoustic flux at the line-formation region, as shown in panels (d) and (f) of Figure 6. The correlation is marginally better for the case of the Mg II  $k_3$  feature. The relatively smaller change of the density of formation in the case of the upper chromospheric Mg II  $k_3$  leads to a better correlation between the synthetic observed velocity fluctuations and the acoustic flux in the atmosphere.

The conclusion from Figure 6 is that the variations in the formation height of the spectral lines in different features is a significant effect when estimating the wave flux in the solar atmosphere, as that will alter the observed wave velocity amplitudes and local densities. Using fixed values for the density will produce results that do not correspond to the true flux at the formation region of the spectral lines. Optimally, we would take this into account when estimating the acoustic flux by employing different densities. However, as we discuss in the following section, sufficient knowledge of the local densities in the chromosphere and their range of variation is still lacking.

### 5.2. Chromospheric Density Estimates Are Model Dependent

Density is the quantity with the highest degree of variability in estimating the acoustic flux in the chromosphere due to its highly corrugated and dynamic structure (Carlsson et al. 2019). As alluded to in the previous subsection, the density at the formation location of the same diagnostics in different regions of the solar atmosphere changes by a few orders of magnitude, as illustrated in Figures 4(b) and (f). In this section we discuss the intrinsic variability of the plasma density at the height of spectral line formation in the different modeling approaches. The variability described here is due to the different line-

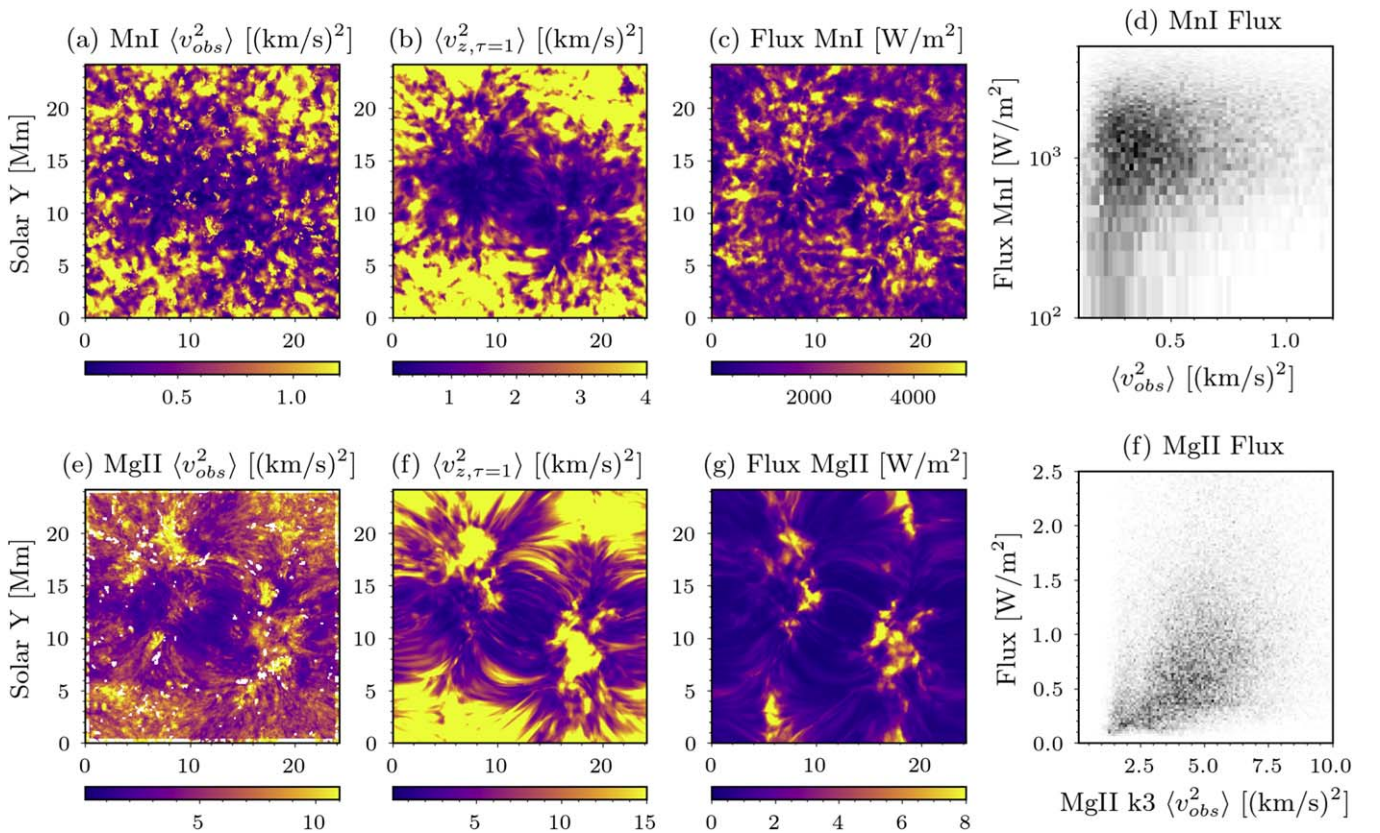


**Figure 6.** Comparison of the synthetic Doppler velocity fluctuations in the Mn I line and Mg II  $k_3$  feature and the wave fluxes at the corresponding heights in the model atmospheres. The top row presents the following Mn I 280.1 nm-derived diagnostics: panel (a) shows the measured synthetic Doppler velocity fluctuations between 5 and 25 mHz, panel (b) shows the vertical velocity oscillatory power between 5 and 25 mHz in the Bifrost simulation at the  $\tau = 1$  height for each column, panel (c) shows the acoustic flux as measured in the simulation at the  $\tau = 1$  height for each column, and panel (d) shows a scatter plot between the quantities in (a) and (c). The bottom row shows the same features but for the Mg II  $k_3$  feature.

formation conditions in the model atmospheres, not intrinsic changes due to the wave perturbations per se.

Figure 7 shows the distribution of plasma densities at the  $\tau = 1$  surface for the Mn I 280.1 nm line in panel (a) and the Mg II  $k_3$  feature in panel (b) for different modeling approaches. The three different models described here are the Bifrost 3D rMHD simulations described in Section 4.2, the RADYN models described in Section 4.1, and the FAL11 semiempirical 1D hydrostatic models described in Fontenla et al. (2011). We use the latest FAL models, since they reproduce the average solar spectra to the best extent, but are in essence very similar to other 1D semiempirical atmospheric models used in previous acoustic wave studies.

For the Bifrost rMHD model, we extracted the corresponding densities at every fifth spatial pixel in both spatial dimensions at 200 s intervals. The distribution of the Bifrost densities are presented as the gray distribution in Figure 7. We also calculated the densities at the two regions of internetwork and active network, marked as the squares in Figure 4. We plot them over the full Bifrost distribution with blue (internetwork) and red (active-network) markers. The formation of the lines in the active network is at higher average plasma densities, which agrees with the previous discussion in Section 4. For the RADYN models, we calculated the Mn I and the Mg II lines for the *model\_3000* run from Paper I for every temporal step, where we have excluded from the synthesis the relaxation time of the simulation. We calculated the density from the other models presented in Paper I that have increasing wave strength,

but the results were similar to the ones presented here. The FAL models A–P, increasing in activity from very quiet internetwork to plage core, are shown with the colored circles on the right. The relative warmth of the color of the marker signifies increasing activity level.

The different modeling approaches produce very different estimates for the plasma density at the line-formation region, as shown in Figure 7. In particular, the Bifrost models exhibit a high level of intrinsic variation of the density in the different solar features. In the case of the Mn I line, the RADYN-derived density corresponds to the quietest FAL models, which is not surprising, given the initial RADYN atmosphere was based on a relaxed FAL B-like model. Comparing the Bifrost density estimates with the 1D model ones, we observe that the active-network regions have a mostly similar density to the ones retrieved from the FAL-based modeling. In the internetwork, the Bifrost models estimate that the density of formation is significantly lower than the one derived from the FAL models, but at some points they exhibit high densities, similar to the ones seen in the enhanced network.

In the case of the Mg II lines, the RADYN models exhibit densities closer to those of the hotter FAL models, opposite from what is seen in the Mn I 280.1 nm line case. However, the more self-consistent Bifrost simulation exhibits significantly lower density than either the FAL or RADYN simulations for both the enhanced network and internetwork.

Using the values of Bifrost simulation-derived densities for flux estimates would lead to lower inferred chromospheric

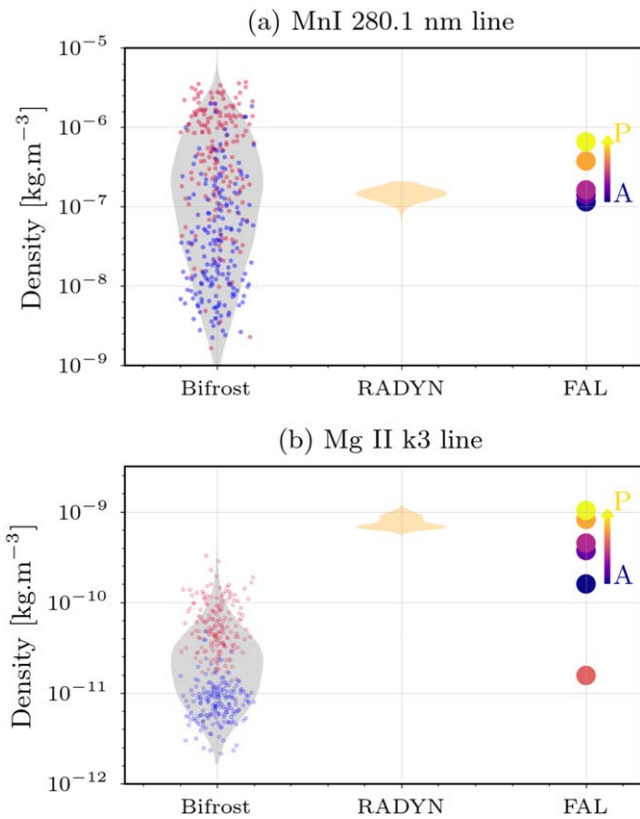


**Figure 7.** Density at the line-formation height for the Mn I 280.1 nm line and the Mg II  $k_3$  feature from different wave-modeling approaches, labeled on the abscissa. The top panel (a) shows the results for the Mn I line and the bottom panel (b) for the Mg II  $k_3$  feature. The data points overlaying the Bifrost density distribution correspond to internetwork (blue) and enhanced-network (red) regions, shown in Figure 4, sampled every 200 s.

wave fluxes when compared with using values based on the FAL models. We do not dispute which density values are more accurate, as the Bifrost models still lack heating and sufficient density in the chromosphere to properly reproduce the observed spectral profiles. Instead, we highlight the systematic biases in different wave flux estimates based on the models used. The large spatial and temporal spread in densities in the more dynamic rMHD models does further indicate that the use of single or few values of density in computing wave fluxes is likely an oversimplification that leads to significant uncertainties.

### 5.3. Uncertainty of the Transmission Coefficient

The attenuation coefficient  $\mathcal{T}$  is the last model-dependent parameter in estimating the wave flux. We define  $\mathcal{T}$  in this work as the ratio of the standard deviation of the observed and actual atmospheric vertical velocities. We take a frequency-averaged approach, as previous work in Paper I calculated  $\bar{\mathcal{T}}$  as a function of frequency and showed that most of the power is at the lower frequencies. To examine its variation in the Bifrost simulations, we calculated the ratio of the standard deviations of the Doppler velocities, derived from the synthetic observations, and the vertical velocities in the simulation at the time-averaged height of the  $\tau=1$  surface. We have filtered the vertical velocities in Fourier space, leaving the frequencies between 5 and 20 mHz. We adopt an averaging of the velocity fluctuation power over the frequency domain for calculating  $\mathcal{T}$ , different from previous work. This makes it more resistant to

noise at the high-frequency limit, which can contribute to the observed Doppler velocities solely due to measurement errors. The attenuation-coefficient maps for both Mn I 280.1 nm (panel (a)) and Mg II  $k_3$  (panel (b)) are presented in Figure 8. The attenuation coefficient varies significantly over the simulation domain and is partially correlated with the type of underlying solar features.

For the Mn I 280.1 nm line the attenuation coefficient is on the order of  $\sim 0.4$  in the internetwork, which might be expected due to the strong variation in the heights being sampled of the Doppler velocity, as discussed in Section 5.1. In the case of the network regions, the attenuation coefficient is closer to unity due to the fact that in these regions the height of formation changes significantly less, as shown in Figure 4(c).

For the Mg II  $k_3$  feature, the attenuation coefficient is in general higher compared with the Mn I lines. In the quieter regions the attenuation coefficient is lower (about  $\sim 0.6$ ) and closer to unity in the network regions. In the case of the Mg II  $k_3$  (panel (b) of Figure 8), we see that the extended fibrillar structures in the simulation are clearly correlated with a higher transmission coefficient.

Panels (c)–(f) of Figure 8 present the PSD distributions of the synthetic observables and the actual plasma vertical velocity. In each panel we plot the PSD of the vertical plasma velocity at the formation height of the spectral line ( $v_{\text{sim}}$ ) as well as the PSD of the Doppler velocity measured in the synthetic observables for the solar region of interest. The lines are the mean of the PSD distributions and the shaded areas represent the 10th–90th percentiles region of the distributions. For the Mn I line on average the power spectra of the observed Doppler velocity signals are attenuated with a constant shift, as seen previously in Paper I and discussed in previous work (Mein & Mein 1976; Bello González et al. 2009). However, for the plage-like regions the power spectra of the true plasma velocity and the one of the observed (synthetic) Doppler velocity are very similar, and in some places the true velocity power exceeds the observed one. This is due to the fact that the passing wave fronts in the atmosphere introduce a jump-like change of the height of formation of the diagnostics, introducing jump-like signals in the measured Doppler velocity. This effect cannot be described with 1D semiempirical atmospheric modeling, and we believe that it is important to include it in accurate estimates of the wave fluxes, as it will increase the attenuation coefficient significantly for brighter regions, leading to lower acoustic flux estimates.

As is evident, the attenuation coefficient varies significantly and may depend in part on the solar feature being observed. This effect cannot be captured by static 1D models and will be definitely misrepresented by 1D hydrodynamic time-dependent models, as the obvious dependence on the simulated magnetic topology of the solar region helps determine its value. Hence, we believe that future estimations of the acoustic flux in the chromosphere should take the complicated nature of the transmission coefficient into consideration.

## 6. Inferring the Acoustic Wave Flux

From the observational data presented in Section 2 and the numerical analysis in Sections 4 and 5, we have required the physical quantities to demonstrate the method for estimating the acoustic flux from IRIS and IBIS observations, based on the synthetic observables derived from the Bifrost models. In Section 5 we showed that the internetwork and the plage

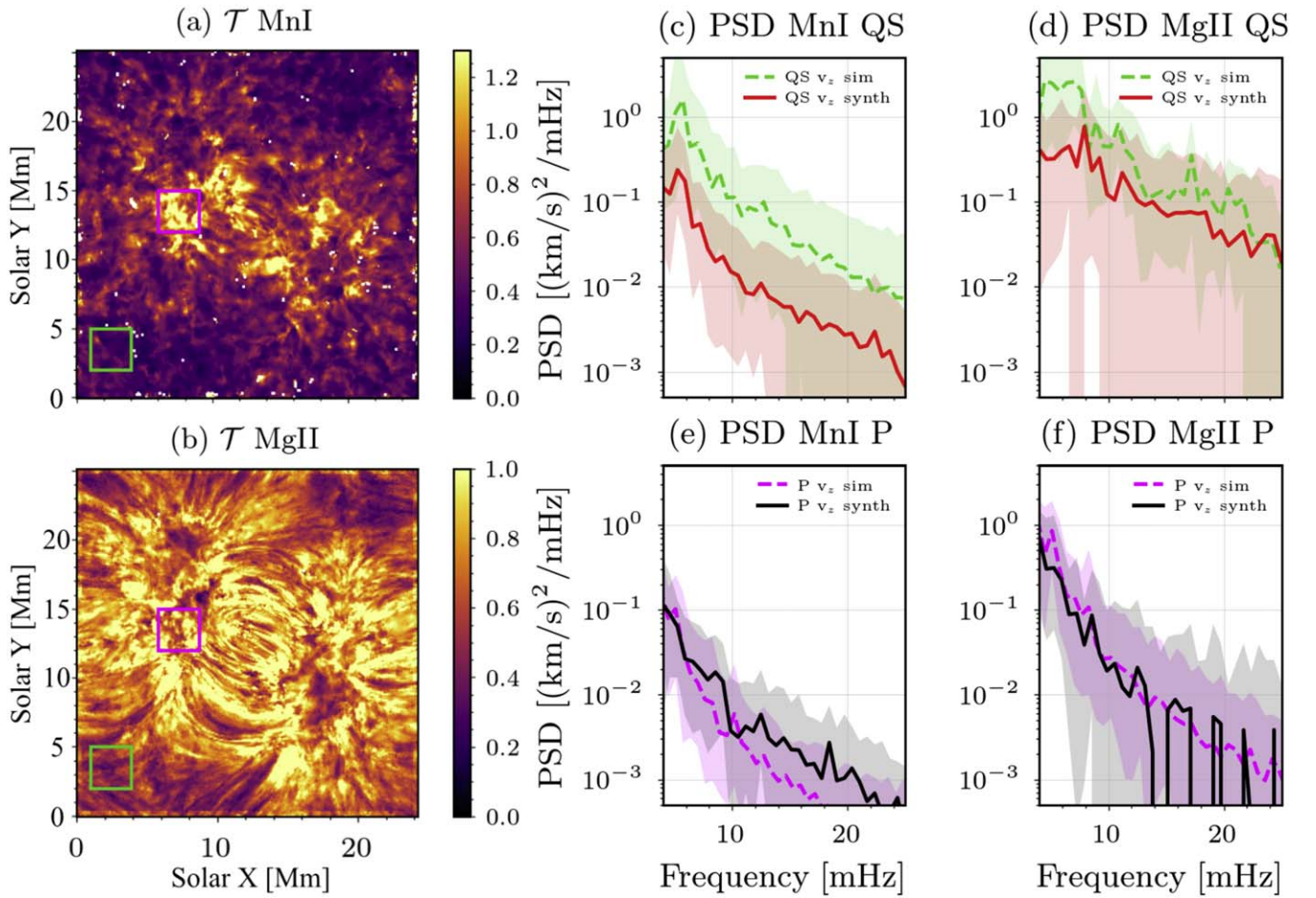


**Figure 8.** Attenuation coefficient  $\mathcal{T}$  maps in the Bifrost simulation for vertical velocity fluctuations between 5 and 20 mHz (panels (a)–(b)) based on the power spectral density (PSD) of the observed and true plasma diagnostics (panels (c)–(f)). The top panel (a) shows the attenuation coefficient in the Mn I 280.1 nm line and the bottom panel (b) shows it for the Mg II  $k_3$  feature. The green and magenta regions correspond to the dark internetwork and enhanced-network regions of interest. Panels (c)–(f) compare the PSD of the vertical velocity oscillatory power in the atmosphere at the formation height of the diagnostic ( $v_{\text{sim}}$ ) and the Doppler velocity oscillatory power in the synthetic observations ( $v_{\text{synth}}$ ) for the quiet Sun and plage regions. Note that the solid/dashed lines are the average of the distributions outlined as the colored squares in panels (a) and (b) and the shaded regions are the 10%/90% percentiles of the distributions.

regions exhibit different line-formation characteristics, such as densities, velocity formation regions, and attenuation of the wave signals, within the Bifrost simulation. In particular, the internetwork exhibits formation of the line that is significantly lower in density and has a lower transmission coefficient compared to the active-network elements.

Despite the variances in density, shown in Figure 7, we chose to use the densities from Bifrost to compute acoustic wave fluxes. The mean formation properties employed for the different spectral lines are listed in Table 3 and were derived from averaging over the representative regions (shown as small boxes) in Figures 4 and 8. The attenuation coefficient values we obtained are significantly closer to unity than what previous authors have cited (Bello González et al. 2009; Abbasvand et al. 2020a), which could be due to the different (and more realistic) modeling approach we employed. However, this will also lead to significantly lower estimates of the energy fluxes.

We used the average formation properties, as derived for regions of the simulation for the observed internetwork and plage regions described in Section 5. To calculate the wave fluxes, we adopt values of the density and the attenuation coefficient for the spectral lines separately for the two regions (shown as squares in Figure 4). The values are listed in Table 3.

**Table 3**  
Density and Attenuation Coefficient Values Used for the Acoustic Flux Estimation

Spectral Line	Density $\rho$ ( $\text{kg m}^{-3}$ )	$\mathcal{T}$
QS Na I $D_1$ 589.6 nm	$6.55 \cdot 10^{-7}$	0.68
QS Mn I 280.1 nm	$2.96 \cdot 10^{-8}$	0.37
QS Ca II 854.2 nm	$3.15 \cdot 10^{-9}$	0.56
QS Mg II $k_3$	$8.55 \cdot 10^{-12}$	0.50
Plage Na I $D_1$ 589.6 nm	$2.04 \cdot 10^{-6}$	0.91
Plage Mn I 280.1 nm	$5.82 \cdot 10^{-7}$	1.03
Plage Ca II 854.2 nm	$1.02 \cdot 10^{-8}$	0.89
Plage Mg II $k_3$	$5.53 \cdot 10^{-11}$	0.80

**Note.** Derived from the averages of the corresponding representative regions in Figure 4.

Figure 9 presents the estimated wave fluxes, based on the calculated properties of the Bifrost simulations for the corresponding solar features. The top panel (a) shows the diagnostics for the internetwork and the bottom panel (b) shows the results for the plage regions. Overplotted is the Bifrost-averaged acoustic flux as a function of height for the two regions for comparison.

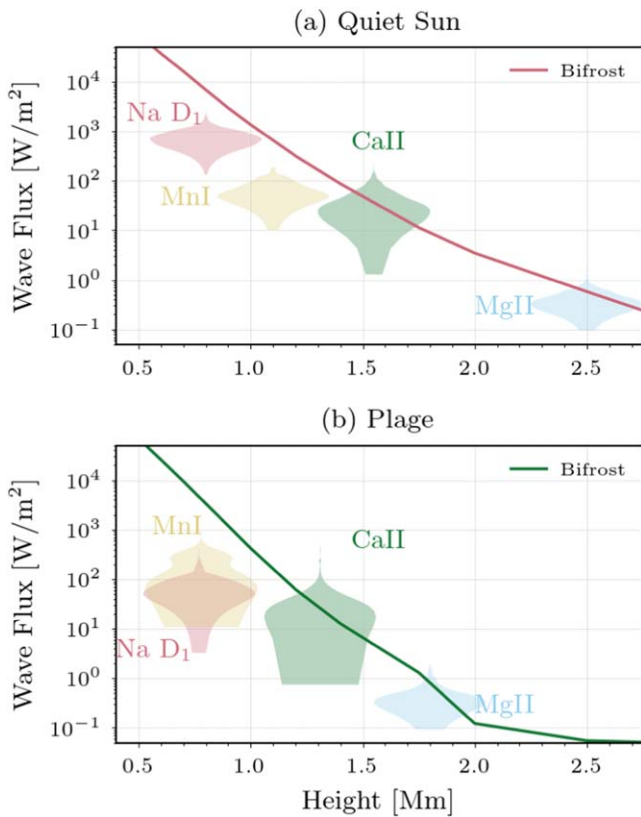


**Figure 9.** Acoustic flux in the different solar regions inferred from the IRIS observations presented in Figure 3. Panel (a) presents the fluxes inferred for the internetwork region and panel (b) presents the fluxes inferred for the plage region. The straight lines show the acoustic fluxes in the Bifrost simulation at the respective height for the solar feature.

For the case of the internetwork, the observation-derived values were generally lower than the acoustic fluxes retrieved directly from the simulations. This can be traced back to the difference in the observed and simulated Doppler velocity distributions in Figure 3. This might be due to a variety of reasons, including the magnetic field topology, incorrect driving of the  $p$ -modes in the bottom boundary of the simulations (Fleck et al. 2021), or incomplete physical treatment of the wave propagation and dissipation.

For the case of the plage observations, we saw that the lower chromosphere diagnostics were orders of magnitudes below the fluxes present in the simulation. Our modeling approach shows that the two independently observed lines of Na I  $D_1$  and the Mn I 280.1 nm exhibit almost the same amount of acoustic flux at the about same formation height, acting as a self-consistency check. The wave fluxes derived from the middle and upper chromospheric diagnostics exhibit values closer to the ones derived from the Bifrost models.

In conclusion, our analysis shows that the observed Doppler velocities are lower than what were derived from the synthetic line profiles calculated from simulations in the four spectral lines with formation heights spanning the chromosphere. Hence, the acoustic fluxes calculated from the observations, based on the simulation results, are also lower and likely insufficient to maintain the solar chromosphere in its quiescent state. This conclusion holds for both the quiet and plage chromospheres, compared to their respective radiative losses (Athay 1976). However, our analysis shows that any such conclusions are highly model dependent. In particular, the

biggest systematic biases are the estimates of the (average-value) densities and the attenuation coefficients.

## 7. Discussion and Conclusions

We present UV observations of waves in the solar chromosphere with the IRIS spacecraft. In particular, we examined the spectral lines of Mn I 280.1 nm (upper photosphere/lower chromosphere) and the Mg II  $k_3$  feature (upper chromosphere). Reduction steps, described in Section 2, enhanced the data and the wave signatures were readily observed. The power spectra of the observed Doppler velocities and line-core intensity oscillations, described in Section 3, exhibit the previously seen ubiquitous power-law distributions. Comparing them with optical diagnostics from previous studies in the literature, we find agreement between the oscillatory properties of UV and optical diagnostics separately observed with IRIS and IBIS.

To interpret these observations, we relied on the 3D rMHD simulation Bifrost, which provided us with a detailed model of the lower solar atmosphere. This model includes detailed physics (non-LTE radiative losses and dynamic hydrogen ionization) important for wave propagation. We used the synthetic observables from Pereira et al. (2013), complemented with our own RH15D synthesis, to understand the formation of the spectral diagnostics in question, described in Section 4. We found that the average density and heights of formation of the spectral lines differ significantly between the internetwork and network regions. Therefore, the height corresponding to the plasma velocity sampled by the Doppler measurement in these lines also changes with the underlying solar feature.

We compared the formation properties of the discussed spectral lines with other wave-modeling approaches used in the literature, the RADYN code and 1D semiempirical atmospheric perturbative approaches. In Section 5, we examined the differing formation properties resulting from the different modeling approaches and how they affect the inferred fluxes. In particular, we discuss how the measured Doppler velocities correspond to actual atmospheric velocities at different heights for the different solar features in Section 5.1. In Bifrost we saw a strong and notable separation in the density of formation for the internetwork and the plage regions. The density of formation is significantly lower than the values found in previous work based on 1D semiempirical models. The value of the transmission coefficient is also significantly lower for the internetwork than for the enhanced-network regions, too. However, it is significantly higher than values used in previous work, leading to lower acoustic wave flux estimates.

Finally, in Section 6 we presented the inferred wave fluxes based on the physical parameters derived from the Bifrost simulations shown in Table 3. We used the values for internetwork and enhanced network separately. In our analysis the wave fluxes inferred from the observations are lower than the ones found in the simulation. In particular, the acoustic fluxes in the lower solar atmosphere, around the formation height of the Mn I and Na  $D_1$  lines, are about a few hundred watts per square meter. At the formation heights of the Mg II  $k_3$  feature, they are on the order of a few watts per square meter. These results do not disagree per se with previous ones in the literature, more than what would be expected due to the systematic modeling biases described in Section 5.

Our work provides us with an example of how more realistic simulations of the solar atmosphere are important for understanding the solar and stellar chromospheres. In particular, we

show that the observed velocity field is not directly related to a singular height in the solar atmosphere. As shown in Figure 6, there is no good correlation between observed velocity amplitudes and the actual wave flux at the height of formation of the line. Because the velocity fluctuations are our key observable for atmospheric energetics, this means that our abilities to derive the amount of acoustic flux is severely limited. We show that the density of formation and transmission coefficients have to be adopted for different solar regions to be able to infer the acoustic flux.

However, given the complex structuring of the chromosphere, we will remain dependent on 3D rMHD models and the derived synthetic observables to provide the basis for determining certain statistical characteristics of different regions of the complex atmosphere. Yet, this makes our derivation of values like the acoustic flux dependent on the veracity and accuracy of those models, which in itself is a challenge to accurately ascertain. It is necessary to be aware of the uncertainties and systematic biases carried forward by values based on these models.

IRIS is a NASA Small Explorer mission developed and operated by LMSAL with mission operations executed at the NASA Ames Research Center and major contributions to downlink communications funded by ESA and the Norwegian Space Centre. Data in this publication were obtained with the facilities of the National Solar Observatory, which is operated by the Association of Universities for Research in Astronomy, Inc. (AURA), under cooperative agreement with the National Science Foundation. The authors would like to thank the anonymous referee, Amanda Alexander, Karen Slater, and Rahul Yadav, whose input greatly improved the manuscript. M. E.M. was supported for part of this work by the DKIST Ambassador Program, funding for which is provided by the National Solar Observatory, a facility of the National Science Foundation, operated under Cooperative Support Agreement number AST-1400405; and in part by a FINESST fellowship with grant No. 80NSSC20K1505. This work utilized resources from the University of Colorado Boulder Research Computing Group, which is supported by the National Science Foundation (grant Nos. ACI-1532235 and ACI-1532236), the University of Colorado Boulder, and Colorado State University.

*Facilities:* IRIS, DST(IBIS).

*Software:* SolarSoft; Matplotlib (Hunter 2007); NumPy (Oliphant 2006); SciPy (Virtanen et al. 2019); h5Py; RH15D (Pereira & Uitenbroek 2015). The Python and IDL scripts utilized for this project are available on the public repository of the author: [https://github.com/momomolnar/IRIS\\_wave\\_signatures](https://github.com/momomolnar/IRIS_wave_signatures) with a copy deposited to Zenodo (Molnar 2023).

## ORCID iDs

Momchil E. Molnar  <https://orcid.org/0000-0003-0583-0516>  
 Kevin P. Reardon  <https://orcid.org/0000-0001-8016-0001>  
 Steven R. Cranmer  <https://orcid.org/0000-0002-3699-3134>  
 Adam F. Kowalski  <https://orcid.org/0000-0001-7458-1176>  
 Ivan Milić  <https://orcid.org/0000-0002-0189-5550>

## References

Abbasvand, V., Sobotka, M., Heinzel, P., et al. 2020a, *ApJ*, 890, 22  
 Abbasvand, V., Sobotka, M., Švanda, M., et al. 2020b, *A&A*, 642, A52  
 Abbasvand, V., Sobotka, M., Švanda, M., et al. 2021, *A&A*, 648, A28  
 Alled, J. C., Hawley, S. L., ABBETT, W. P., & Carlsson, M. 2005, *ApJ*, 630, 573

Alled, J. C., Kowalski, A. F., & Carlsson, M. 2015, *ApJ*, 809, 104  
 Anan, T., Schad, T. A., Kitai, R., et al. 2021, *ApJ*, 921, 39  
 Aschwanden, M. J. 2019, *New Millennium Solar Physics*, Vol. 458 (Switzerland: Springer Natur)  
 Athay, R. G. 1976, *The solar chromosphere and corona: Quiet sun*, Vol. 53 (Dordrecht: Reidel)  
 Bello González, N., Flores Soriano, M., Kneer, F., & Okunev, O. 2009, *A&A*, 508, 941  
 Bergemann, M., Gallagher, A. J., Eitner, P., et al. 2019, *A&A*, 631, A80  
 Bertschinger, E., & Chevalier, R. A. 1985, *ApJ*, 299, 167  
 Biermann, L. 1946, *NW*, 33, 118  
 Bjørgen, J. P., Leenaarts, J., Rempel, M., et al. 2019, *A&A*, 631, A33  
 Bray, R. J., & Loughhead, R. E. 1974, *The solar chromosphere* (London: Chapman and Hall)  
 Carlsson, M., De Pontieu, B., & Hansteen, V. H. 2019, *ARA&A*, 57, 189  
 Carlsson, M., Hansteen, V. H., de Pontieu, B., et al. 2007, *PASJ*, 59, S663  
 Carlsson, M., Hansteen, V. H., Gudiksen, B. V., Leenaarts, J., & De Pontieu, B. 2016, *A&A*, 585, A4  
 Carlsson, M., & Stein, R. F. 1992, *ApJL*, 397, L59  
 Cavallini, F. 2006, *SoPh*, 236, 415  
 da Silva Santos, J. M., Danilovic, S., Leenaarts, J., et al. 2022, *A&A*, 661, A59  
 de Pontieu, B. 2004, in Proc. of “SOHO 13 - Waves, Oscillations and Small-Scale Transient Events in the Solar Atmosphere: A Joint View from SOHO and TRACE” (Paris: ESA), 25  
 De Pontieu, B., Title, A. M., Lemen, J. R., et al. 2014, *SoPh*, 289, 2733  
 Díaz Baso, C. J., de la Cruz Rodríguez, J., & Leenaarts, J. 2021, *A&A*, 647, A188  
 Felipe, T., Kuckein, C., & Thaler, I. 2018, *A&A*, 617, A39  
 Felipe, T., & Socas-Navarro, H. 2023, *A&A*, 670, A133  
 Fleck, B., Carlsson, M., Khomenko, E., et al. 2021, *RSPTA*, 379, 20200170  
 Fontenla, J. M., Harder, J., Livingston, W., Snow, M., & Woods, T. 2011, *JGRD*, 116, D20108  
 Fossum, A., & Carlsson, M. 2005, *Natur*, 435, 919  
 Fossum, A., & Carlsson, M. 2006, *ApJ*, 646, 579  
 Gudiksen, B. V., Carlsson, M., Hansteen, V. H., et al. 2011, *A&A*, 531, A154  
 Heggland, L., Hansteen, V. H., De Pontieu, B., & Carlsson, M. 2011, *ApJ*, 743, 142  
 Hofmann, R. A., Reardon, K. P., Milic, I., et al. 2022, *ApJ*, 933, 244  
 Hunter, J. D. 2007, *CSE*, 9, 90  
 Innes, D. E., Inhester, B., Axford, W. I., & Wilhelm, K. 1997, *Natur*, 386, 811  
 Jefferies, S. M., Fleck, B., Murphy, N., & Berrilli, F. 2019, *ApJL*, 884, L8  
 Kayshap, P., Murawski, K., Srivastava, A. K., Musielak, Z. E., & Dwivedi, B. N. 2018, *MNRAS*, 479, 5512  
 Kurucz, R. L. 2018, in ASP Conf. Ser. 515, *Workshop on Astrophysical Opacities* (San Francisco, CA: ASP), 47  
 Leenaarts, J., Pereira, T., & Uitenbroek, H. 2012, *A&A*, 543, A109  
 Leenaarts, J., Pereira, T. M. D., Carlsson, M., Uitenbroek, H., & De Pontieu, B. 2013, *ApJ*, 772, 90  
 Leenaarts, J., Ruten, R. J., Reardon, K., Carlsson, M., & Hansteen, V. 2010, *ApJ*, 709, 1362  
 Linsky, J. L. 2017, *ARA&A*, 55, 159  
 Louis, R. E., Prasad, A., Beck, C., Choudhary, D. P., & Yalim, M. S. 2021, *A&A*, 652, L4  
 Mein, N., & Mein, P. 1976, *SoPh*, 49, 231  
 Molnar, M. E., Reardon, K. P., Chai, Y., et al. 2019, *ApJ*, 881, 99  
 Molnar, M. E., Reardon, K. P., Cranmer, S. R., et al. 2021, *ApJ*, 920, 125  
 Molnar, M. 2023, *momomolnar/IRIS\_wave\_signatures: Scripts used for Molnar, et al. 2023 ApJ, v1.0.0, Zenodo, doi:10.5281/zenodo.7634027*  
 Morosin, R., de la Cruz Rodríguez, J., Díaz Baso, C. J., & Leenaarts, J. 2022, *arXiv:2203.01688*  
 Oliphant, T. 2006, *NumPy: A guide to NumPy* (USA: Trelgol Publishing), <http://www.numpy.org>  
 Pereira, T. M. D., Leenaarts, J., De Pontieu, B., Carlsson, M., & Uitenbroek, H. 2013, *ApJ*, 778, 143  
 Pereira, T. M. D., & Uitenbroek, H. 2015, *A&A*, 574, A3  
 Pietrow, A. G. M., Kiselman, D., de la Cruz Rodríguez, J., et al. 2020, *A&A*, 644, A43  
 Reardon, K. P., & Cavallini, F. 2008, *A&A*, 481, 897  
 Reardon, K. P., Lepreti, F., Carbone, V., & Vecchio, A. 2008, *ApJL*, 683, L207

- Rimmele, T. R., Warner, M., Keil, S. L., et al. 2020, *SoPh*, **295**, 172
- Roupe van der Voort, L., De Pontieu, B., Scharmer, G. B., et al. 2017, *ApJL*, **851**, L6
- Sadeghi, R., & Tavabi, E. 2022, *MNRAS*, **512**, 4164
- Schatzman, E. 1949, *AnAp*, **12**, 203
- Scherrer, P. H., Schou, J., Bush, R. I., Kosovichev, A. G., Bogart, R. S., et al. 2012, *SoPh*, **275**, 207
- Schou, J., Scherrer, P. H., Bush, R. I., et al. 2012, *SoPh*, **275**, 229
- Sobotka, M., Heinzel, P., Švanda, M., et al. 2016, *ApJ*, **826**, 49
- Socas-Navarro, H. 2005, *ApJL*, **633**, L57
- Tousey, R. 1967, *ApJ*, **149**, 239
- Uitenbroek, H. 2001, *ApJ*, **557**, 389
- Ulmschneider, P., Rammacher, W., Musielak, Z. E., & Kalkofen, W. 2005, *ApJL*, **631**, L155
- Vecchio, A., Cauzzi, G., Reardon, K. P., Janssen, K., & Rimmele, T. 2007, *A&A*, **461**, L1
- Virtanen, P., Gommers, R., Oliphant, T. E., et al. 2019, arXiv:1907.10121
- Wedemeyer-Böhm, S., Steiner, O., Bruls, J., & Rammacher, W. 2007, in *Astronomical Society of the Pacific Conference Series*, Vol. 368, *The Physics of Chromospheric Plasmas*, ed. P. Heinzel, I. Dorotovič, & R. J. Rutten 93
- Withbroe, G. L., & Noyes, R. W. 1977, *ARA&A*, **15**, 363
- Wunnenberg, M., Kneer, F., & Hirzberger, J. 2002, *A&A*, **395**, L51
- Zaqarashvili, T. V., & Skhirtladze, N. 2008, *ApJL*, **683**, L91